ACS NANO

www.acsnano.org

ARTICLE

Voltage Modulation of Nanoplasmonic Metal Luminescence from Nano-Optoelectrodes in Electrolytes

Yuming Zhao, Chuan Xiao, Elieser Mejia, Aditya Garg, Junyeob Song, Amit Agrawal, and Wei Zhou*

Cite This: *ACS Nano* 2023, 17, 8634–8645

Read Online

ACCESS | Metrics & More | Article Recommendations | Supporting Information

ABSTRACT: Metallic nanostructures supporting surface plasmon modes can concentrate optical fields and enhance luminescence processes from the metal surface at plasmonic hotspots. Such nanoplasmonic metal luminescence contributes to the spectral background in surface-enhanced Raman spectroscopy (SERS) measurements and is helpful in bioimaging, nanothermometry and chemical reaction monitoring applications. Although there is growing interest in nanoplasmonic metal luminescence, its dependence on voltage modulation has received limited attention in research investigations. Also, the hyphenated electrochemical surface-enhanced Raman spectroscopy (EC-SERS) technique typically ignores voltage-dependent spectral background information associated with nanoplasmonic metal luminescence due to limited mechanistic understanding and poor measurement reproducibility. Here, we report a combined experiment and theory study on dynamic voltage-modulated nanoplasmonic metal luminescence from hotspots at the electrode−electrolyte interface using multiresonant nanolaminate nano-optoelectrode arrays. Our EC-SERS measurements under 785 nm continuous wavelength laser excitation demonstrate that short-wavenumber nanoplasmonic metal luminescence associated with plasmon-enhanced electronic Raman scattering (PE-ERS) exhibits a negative voltage modulation slope (up to ≈30% V^{-1}) in physiological ionic solutions. Furthermore, we have developed a phenomenological model to intuitively capture the plasmonic, electronic, and ionic characteristics at the metal−electrolyte interface to understand the observed dependence of the PE-ERS voltage modulation slope on voltage polarization and ionic strength. The current work represents a critical step toward the general application of nanoplasmonic metal luminescence signals in optical voltage biosensing, hybrid optical-electrical signal transduction, and interfacial electrochemical monitoring.

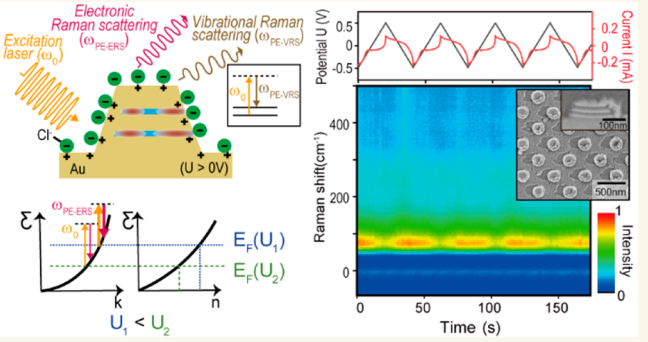

KEYWORDS: *electrochemical surface-enhanced Raman spectroscopy (EC-SERS), nanoplasmonic metal luminescence, plasmon-enhanced electronic Raman scattering (PE-ERS), plasmon-enhanced vibrational Raman scattering (PE-VRS), nano-optoelectrodes, multiresonant plasmonics, interfacial capacitance*

INTRODUCTION

Metallic nanostructures can support surface plasmon modes and concentrate optical fields to enhance nanoscale luminescence processes ranging from spontaneous and stimulated emission, resonant and nonresonant Raman scattering, and nonlinear harmonic generation.[1−7] Among various applications using plasmon-enhanced luminescence, surface-enhanced Raman spectroscopy (SERS) has received enormous attention as a compact biochemical detection technique with combined vibrational fingerprint specificity and plasmonic hotspot sensitivity.[8] In addition to discrete plasmon-enhanced vibrational Raman scattering (PE-VRS) peaks from molecules at hotspots, a measured SERS spectrum often has a broad continuous emission background, typically subtracted and neglected in biochemical analyses. Recent studies reveal that the SERS background can originate from plasmon-enhanced metal luminescence at hotspots.[9,10] Moreover, over the past decade, there has been a rising interest in investigating

Received: February 15, 2023
Accepted: April 18, 2023
Published: April 24, 2023

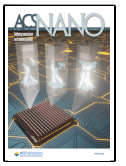

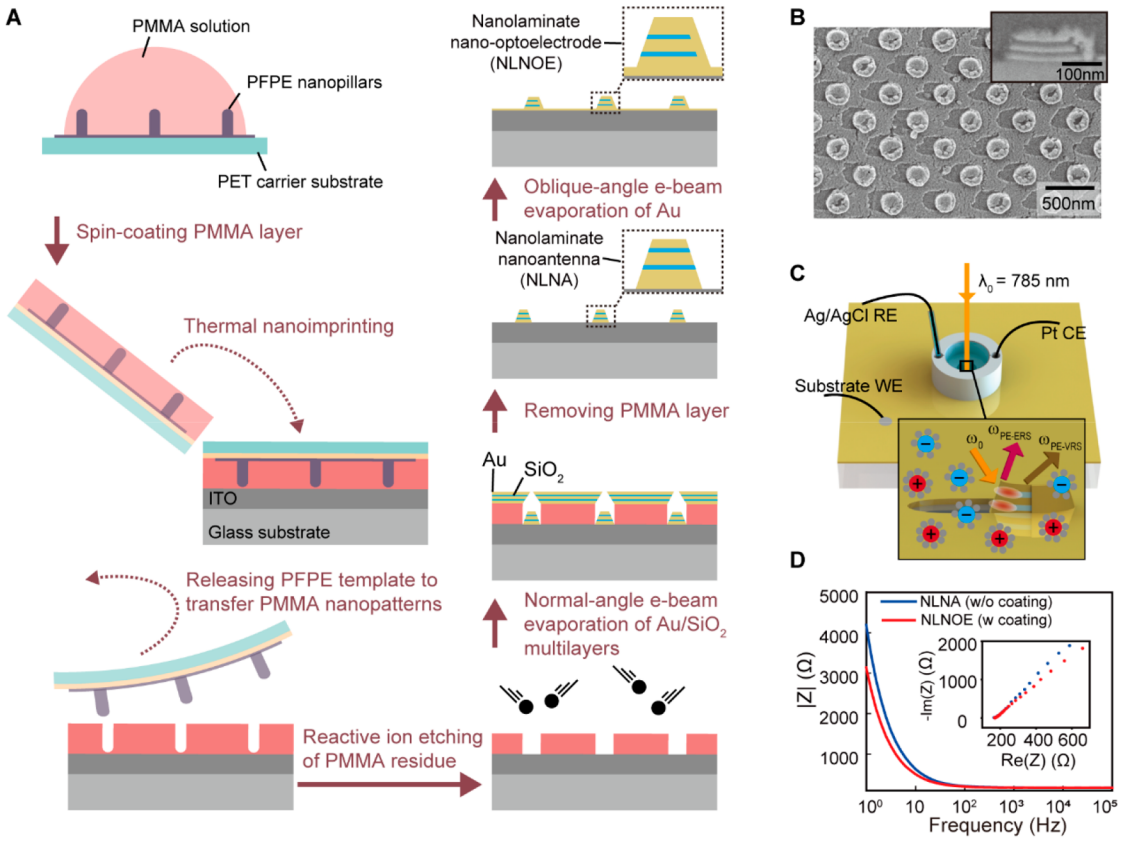

Figure 1. Nanolaminate nano-optoelectrode (NLNOE) with electrically connected metal−insulator−metal (MIM) multinanogap nanocavity plasmonic hotspots. (A) The fabrication scheme of creating periodic arrays of NLNOEs consisting of multilayered Au/SiO_2 nanolaminate nanoantennas (NLNAs) with a thin Au layer coated on its side wall by oblique-angle e-beam evaporation. (B) Top-down and cross-sectional (inset) SEM images of fabricated NLNOEs. (C) The scheme of *in situ* electrochemical SERS measurements of NLNOEs in the electrolyte with a three-electrode configuration under 785 nm laser excitation. The inset scheme shows that the electrically connected multinanogap nanocavity hotspots in the NLNOE can generate plasmon-enhanced electronic Raman scattering (PE-ERS) and plasmon-enhanced vibrational Raman scattering (PE-VRS) signals at the metal−electrolyte interface under laser excitation. (D) Electrochemical impedance spectroscopy (EIS) measured Bode magnitude plots and Nyquist plots for the NLNOE (with sidewall Au coating) and NLNA (without sidewall Au coating) samples in 1× phosphate-buffered saline (PBS).

plasmon-enhanced metal luminescence for applications ranging from bioimaging to nanothermometry and chemical reaction monitoring.[11−17] Nevertheless, the exact mechanism of plasmonic metal luminescence is still under debate and can involve several possible pathways, including interband photoluminescence,[18,19] intraband photoluminescence,[20−23] and electronic Raman scattering (ERS).[9,24−27] Moreover, despite studies on the effects of continuous-wave (cw) or pulsed excitation conditions, excitation wavelengths, temperature, metal geometries, and metal types,[9,11,12,20−25,27−30] little attention has been paid to investigating how the plasmonic metal luminescence depends on the applied voltage modulation at hotspots.

In a different but related field, the hyphenated electrochemical surface-enhanced Raman spectroscopy (EC-SERS) has emerged as a powerful nanoscale spectroelectrochemistry technique to simultaneously monitor molecular fingerprint information and electrochemical activities at the metal−electrolyte interface under voltage modulation,[31−33] which has applications in interfacial spectroelectrochemistry analyses[34−36] and biochemical sensing.[37−39] Compared to SERS, EC-SERS incorporates charge transfer and redox reactions at the metal−liquid interface. These additional effects influence the material type, morphology, charge density, and permittivity at the nanostructured metal−liquid interface, directly or indirectly affecting both the PE-VRS and the background emission processes. While several studies have shown a correlation between voltage and plasmon-enhanced metal luminescence within electrochemical setups,[40−42] a comprehensive understanding of the connection between electrode interfacial behavior and the microscopic representation of plasmon-enhanced metal luminescence remains elusive. Furthermore, most EC-SERS studies have employed nonuniform plasmonic devices based on metal nanoparticle aggregates or roughened metal electrodes with randomly distributed or mechanically unstable plasmonic hotspots,[31,32,36−39,43] limiting EC-SERS measurement reproducibility for reliable analysis of voltage-dependent spectral background information.

Here, we report a combined experiment and theory study on dynamic voltage-modulated nanoplasmonic metal luminescence from hotspots at the electrode−electrolyte interface using multiresonant nanolaminate nano-optoelectrode (NLNOE) arrays. Using EC-SERS measurements under 785 nm laser excitation, we demonstrate that NLNOEs consisting of vertically stacked and electrically connected Au-SiO_2−Au nanocavities can produce voltage-sensitive (up to ≈30% V^{-1}) short-wavenumber (≈87 cm^{-1}) nanoplasmonic metal luminescence signals associated with plasmon-enhanced electronic

https://doi.org/10.1021/acsnano.3c01491
ACS Nano 2023, 17, 8634−8645

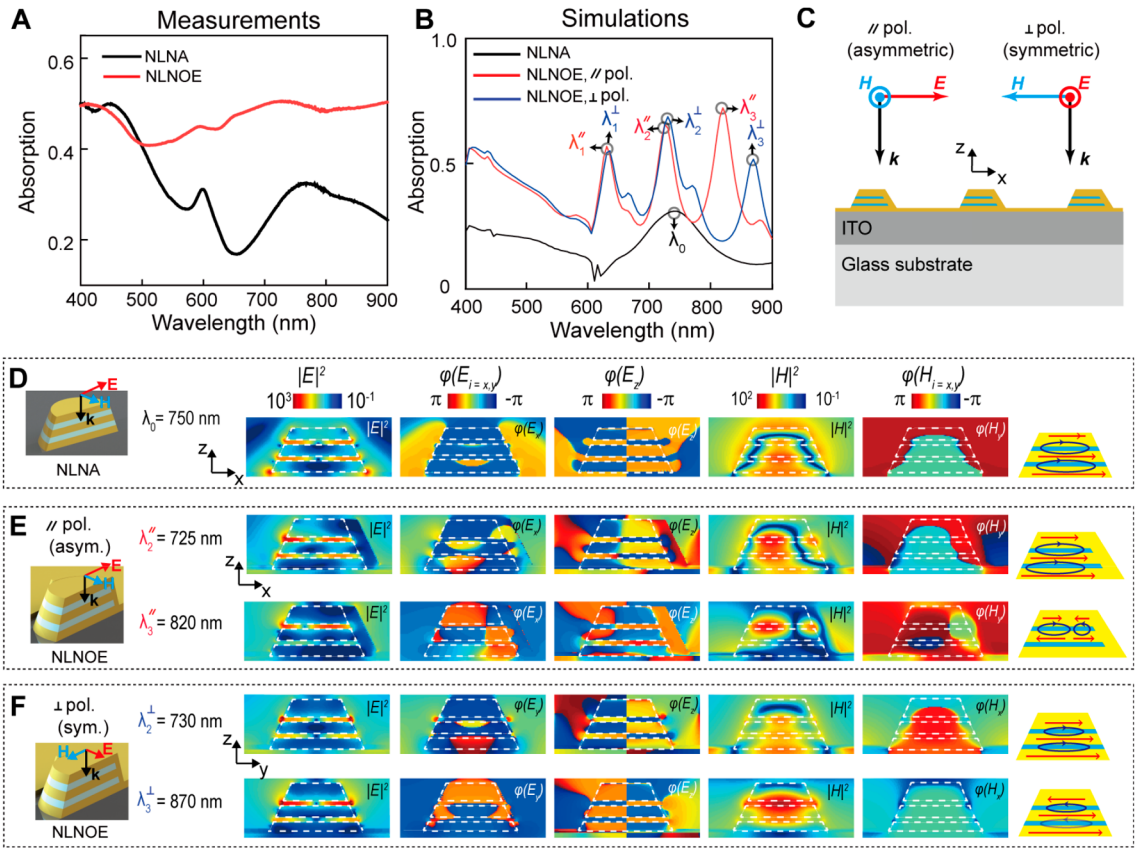

Figure 2. Multiresonant optical characteristics of NLNOEs. (A) Measured and (B) FDTD-calculated absorption spectra for NLNOE and the NLNA. (C) Light illumination scheme in FDTD simulations under parallel ∥ (asymmetric) and perpendicular ⊥ (symmetric) polarization excitation configurations regarding the mirror-symmetry $x-z$ plane for NLNOEs. (D–F) FDTD-calculated near-field distribution maps of $|E|^2$, $\varphi(E_{i=x,y})$, $\varphi(E_z)$, $|H|^2$, and $\varphi(H_{i=y,x})$ in the $x-z$ or $y-z$ plane for the resonant modes for (D) the NLNA at λ_0 = 750 nm, (E) the NLNOE at $\lambda_2^{\parallel}$ = 725 nm and $\lambda_3^{\parallel}$ = 820 nm under ∥ polarization light, and (F) the NLNOE at $\lambda_2^{\perp}$ = 730 nm and $\lambda_3^{\perp}$ = 870 nm under ⊥ polarization light.

Raman scattering (PE-ERS) in physiological ionic solutions. Furthermore, we have developed a phenomenological model that can capture plasmonic, electronic, and ionic characteristics at the metal–electrolyte interface to understand several experimental observations, including: (i) negative voltage modulation slope for PE-ERS signals, (ii) an abrupt change in PE-ERS voltage modulation slope by switching electrode voltage polarity, and (iii) reduction of PE-ERS voltage modulation slope amplitude with increasing ionic strength. Our model intuitively reveals that (i) the observed voltage sensitivity of PE-ERS metal luminescence signals originates from the spatial overlap between the metal electronic Debye length (d_D^m) and the penetration depth ($d_{SP}^m/4$) of fourth power of surface plasmon field ($|E_S|^4$) within the metal surface exposed to the electrolyte at hotspots, and (ii) voltage-sensitive metal luminescence from electrically connected hotspots in nano-optoelectrodes can serve as probe signals to monitor the dynamic changes in microscopic capacitive characteristics (e.g., local electrolyte Debye length d_D^l, local dielectric permittivity ϵ_D^l) at the electrode–electrolyte interface.

RESULTS AND DISCUSSION

Fabrication and Characterization of Nanolaminate Nano-Optoelectrodes. In many biomedical and environmental applications using SERS/EC-SERS, it is highly desirable to employ near-infrared (NIR) laser excitation and Au-based plasmonic devices to (i) minimize molecular autofluorescence background, (ii) reduce cellular phototoxicity, (iii) ensure chemical stability and biocompatibility, and (iv) increase optical penetration depth in measurements. Therefore, in this work, we developed Au-based NLNOEs with NIR multiresonant responses to conduct SERS/EC-SERS measurements under NIR laser excitation at 785 nm. Moreover, several studies suggest that PE-ERS can be the dominant pathway for low-wavenumber nanoplasmonic metal luminescence from metal–insulator–metal (MIM) nanogap cavities under NIR laser excitation because of the difficulty in achieving (i) intraband photoluminescence with the small incident photon energy and (ii) intraband photoluminescence with significant momentum mismatch in real-state electronic transitions across the dispersive sp-band.[9,24,26] Our recent work has further demonstrated that low-wavenumber ($\lesssim$100 cm^{-1}) nanoplasmonic metal luminescence associated with PE-ERS signals from MIM nanogap cavities under the NIR laser excitation experience an $|E|^4$ enhancement factor[24] to serve as an internal standard for spatial and temporal calibration of PE-VRS signals in SERS measurements.[26,44]

As shown in Figure 1A, we employed our recently developed reverse nanoimprinting technique[45] to create large area, uniform NLNOE arrays on planar substrates. First, a reusable inverse template of perfluoropolyether (PFPE) nanopillar arrays on the polyethylene terephthalate (PET) carrier substrate was replicated from a silicon master of square nanowell array (diameter ≈ 120 nm, depth ≈ 300 nm, and

https://doi.org/10.1021/acsnano.3c01491
ACS Nano 2023, 17, 8634–8645

periodicity ≈ 400 nm) by nanoimprint lithography. With low surface energy and relatively high young modulus, the PFPE template can allow a reverse nanoimprinting process to create the deposition mask of poly(methyl methacrylate) (PMMA) nanohole array patterns on planar substrates. Second, we spin-coated diluted PMMA solution on hydrophobic PFPE nanopillar array. Third, we performed thermal nanoimprinting to transfer the PMMA nanowell arrays onto an indium−tin-oxide (ITO) coated glass slide. Then, we converted PMMA nanowells to nanoholes by reactive ion etching (RIE), yielding a deposition mask for electron-beam (e-beam) evaporation of alternating Au (≈25 nm) and SiO_2 (≈10 nm) thin-film layers. Next, we dissolved PMMA in anisole to lift off the deposited excess material layer and reveal a discrete array of nano-laminate nanoantennas (NLNAs) with multilayered metal−insulator−metal (MIM) nanocavities. Finally, an angled (≈50°) deposition by e-beam evaporation was performed to form a sidewall coating of ≈30 nm thick Au on one side of NLNAs, connecting the nanocavities to the conductive substrate ground to yield uniform NLNOE arrays. Crucially, the sidewall coating from angled e-beam deposition can enable voltage modulation of hotspots in EC-SERS measurements while leaving one side of NLNOEs uncovered to expose plasmonic nanocavity hotspots to the electrolyte environment. In Figure 1B, the top-view and cross-section scanning electron microscopy (SEM) images of NLNOE arrays reveal diagonally oriented elliptic Au nanohole arrays at the base of NLNOE due to the shadowing effect during the angled deposition.

Figure 1C illustrates the setup for *in situ* EC-SERS measurements of the NLNOE sample, which also serves as a working electrode (WE). The plastic well of the EC cell was mounted directly onto the NLNOE-based WE substrate with an overall metal−electrolyte interface area of ≈1 cm^2. The plastic well contained two inlets with a platinum wire counter electrode (CE) and an Ag/AgCl (saturated in KCl) reference electrode (RE). We conducted *in situ* EC-SERS measurements of NLNOEs with a cw near-infrared (NIR) laser excitation at 785 nm to collect the backscattered PE-ERS and PE-VRS signals using a confocal microscope. Using a potentiostat, we first conducted electrochemical impedance spectroscopy (EIS) for NLNA (without a single-sided Au coating) and NLNOE (with a single-sided Au coating) samples on the ITO glass substrates (Figure 1D). EIS measurements show a large impedance at low frequencies that decreases exponentially as the frequency increases for both NLNA and NLNOE samples. Notably, the EIS spectra reveal smaller impedance values for NLNOE than the NLNA sample, manifesting an increased capacitance due to an increased electrode surface area from the metal sidewall coating. The capacitive reactance, however, is inversely proportional to capacitance; hence, overall impedance shifts downward at low frequencies with the metal sidewall coating.

Optical Characteristics of Nanolaminate Nano-Opto-electrodes. To investigate how the metal sidewall coating influences the optical properties, we performed visible-NIR reflection (R) and transmission (T) measurements for NLNA and NLNOE samples with an area of ≈2 cm^2 using a UV−visible−near-infrared (NIR) spectrophotometer under unpolarized white light illumination. Both reflectance and transmittance measurements employed an integrating sphere with an incidence angle of ≈3.3° to collect specular and diffuse light from the samples. Figure 2A shows the retrieved absorption spectra ($A = 1 - T - R$) for NLNA and NLNOE samples. The NLNA sample shows a narrow Fano-like asymmetric resonant peak at ≈600 nm and a broad resonant peak at ≈780 nm with peak absorption of ≈30%, while the NLNOE sample shows a significantly higher absorption of ≈40% to ≈50% across a broad spectral range from ≈500 nm to ≈900 nm.

To understand the different measurement optical responses between NLNA and NLNOE samples, we employed finite-difference time-domain (FDTD) method (see Methods) to calculate their far-field and near-field characteristics with nominal geometries estimated from SEM images in Figure 1B. We used a periodic boundary condition in the x and y directions with a periodicity of 400 nm and a perfectly matched layer (PML) boundary condition in the z-direction. For the FDTD simulations of the NLNOE, we define the $x-z$ plane as the plane for the line-of-sight oblique-angle e-beam deposition of single-sided metal coatings on the sidewall. Unlike NLNA, NLNOE with a single-sided metal coating has a broken mirror symmetry and therefore exhibits different optical responses under normal-incidence plane-wave illuminations with parallel (∥) and perpendicular (⊥) polarizations (Figure 2C). FDTD-calculated far-field absorption spectra for NLNA and NLNOE in Figure 2B reveal several crucial features. First, consistent with the measurements in Figure 2A, FDTD calculations for the NLNA exhibit a narrow Fano-like asymmetric feature at ≈600 nm due to periodic lattice diffraction[46,47] and a broad resonant feature at ≈750 nm with an absorption peak of ≈30%. Second, FDTD calculations confirm that the NLNOE exhibits input polarization dependent multiresonant optical response due to the broken mirror symmetry. Third, in contrast to the NLNOE's broadband absorption responses (≈40% to ≈50%) in measurements, FDTD calculations show multiple narrow resonant features with a higher peak absorption of ≈50% to ≈70% under parallel ($\lambda_1^{\parallel} \approx 610$ nm, $\lambda_2^{\parallel} \approx 725$ nm, $\lambda_3^{\parallel} \approx 820$ nm) and perpendicular ($\lambda_1^{\perp} \approx 610$ nm, $\lambda_2^{\perp} \approx 730$ nm, $\lambda_3^{\perp} \approx 870$ nm) polarized illumination. Last, in agreement with the measurements, FDTD calculations manifest that the NLNOE can induce a roughly 2-fold higher broadband absorption than the NLNA without the single-sided metal coating under either ∥ or ⊥ polarized illumination. We note that NLNOE simulations produce narrower resonant features than the measurements due to (i) the inhomogeneous broadening effect from geometric variations among periodic unit cells in the fabricated sample and (ii) the homogeneous broadening effect from extra optical losses from nanostructure surface roughness and plasmon damping from interfacial ≈0.5 nm thick Cr adhesion layer between Au and SiO_2 layers. Thus, multiple narrow plasmonic peaks in NLNOE simulations can blur and merge into a broad absorption feature in the measurements.

To investigate the microscopic origin behind distinct far-field optical responses, we calculated the near-field distribution maps of field intensities $|\boldsymbol{E}|^2$ and $|\boldsymbol{H}|^2$, and phases $\varphi(\boldsymbol{E}_i)$ and $\varphi(\boldsymbol{H}_i)$ for representative modes supported in NLNA and NLNOE arrays (Figure 2D−F). The FDTD-calculated 2D near-field plots can reveal several critical points. First, as shown in Figure 2D, the broad resonance in the NLNA at $\lambda_0 \approx 750$ nm exhibits (i) electric dipole (ED) characteristics with an in-phase $\varphi(\boldsymbol{E}_x)$ distribution in three Au nanodisks, and (ii) magnetic dipole (MD) characteristics with an in-phase $\varphi(\boldsymbol{H}_y)$ distribution across the two vertically stacked Au-SiO_2−Au nanocavities, and thus is a hybridized electrical dipole−magnetic dipole (ED-MD) plasmonic mode.[48,49] Second, for the NLNOE under ∥ and ⊥ polarized illumination, both

https://doi.org/10.1021/acsnano.3c01491
ACS Nano 2023, 17, 8634−8645

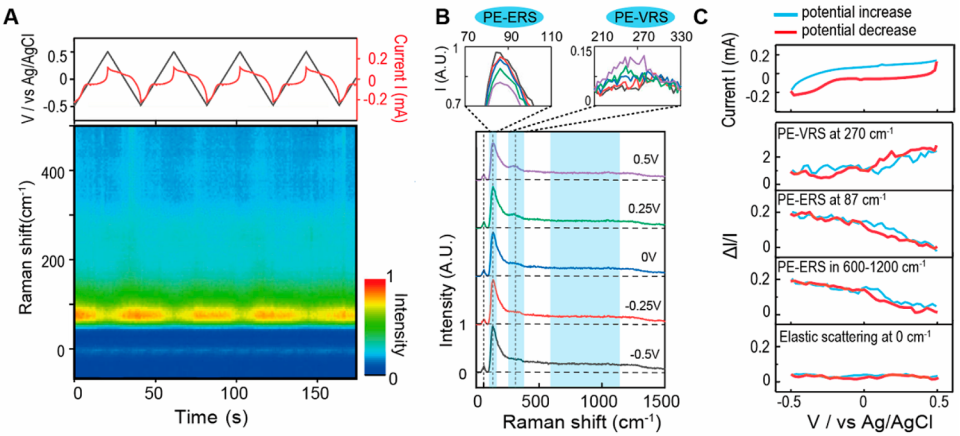

Figure 3. Electrode potential modulation of PE-ERS and PE-VRS signals from NLNOEs in the electrolyte. (A) Time-dependent current measurements (top) under cyclic voltage (CV) sweeping between −0.5 and 0.5 V and time-dependent light emission spectra (bottom) under 785 nm laser excitation from the NLNOE sample in the 1× PBS. (B) The measured light emission spectra (bottom) from the NLNOE sample in the 1× PBS under 785 nm laser excitation at different applied potentials between −0.5 and 0.5 V and the corresponding zoomed-in view of PE-ERS pseudo peaks around ≈87 cm^{-1} (top left) and PE-VRS features around ≈270 cm^{-1} for Au−Cl bonds (top right) at different potentials. (C) The cyclic potential-dependent current (top) and normalized light emission intensities (bottom) for PE-VRS Au−Cl peak at ≈270 cm^{-1}, PE-ERS pseudo peak at ≈87 cm^{-1}, PE-ERS broad continuum integrated between 600 and 1200 cm^{-1}, and elastic scattering peak at ≈0 cm^{-1}. Note: The coefficient of variations for positive and negative PE-ERS modulation slopes are 4.1% and 3.7%, respectively.

modes at $\lambda_1^{\parallel} \approx 610$ nm and $\lambda_1^{\perp} \approx 610$ nm, originate from the hybridization between the (±1,0) surface plasmon polariton (SPP) Bloch modes at Au nanohole array and ED plasmonic modes in Au nanodisks (Figures S1 and S2, Supporting Information). Third, for the NLNOE under ∥ and ⊥ polarized illumination, both modes at $\lambda_2^{\parallel} \approx 725$ nm (Figure 2E, top) and $\lambda_2^{\perp} \approx 730$ nm (Figure 2F, top) exhibit near-field characteristics of hybridized ED-MD plasmonic modes. Next, under ∥ polarized illumination, the excited mode at $\lambda_3^{\parallel} \approx 820$ nm (Figure 2E, bottom) exhibits magnetic quadrupole (MQ) characteristics with an out-of-phase $\varphi(\boldsymbol{H}_y)$ distribution in the top Au-SiO_2−Au nanocavity, manifesting that the single-side metal coating can break the mirror symmetry to lift the degeneracy of MD modes at MIM nanocavity edges and allow their out-of-phase coupling. Lastly, under ⊥ polarized illumination, the excited mode at $\lambda_3^{\perp} \approx 870$ nm (Figure 2F, bottom) exhibits (i) electric quadrupole (EQ) characteristics with an out-of-phase $\varphi(\boldsymbol{E}_y)$ distribution between the top Au disk and the two Au disks below and (ii) MD characteristics with in-phase $\varphi(\boldsymbol{H}_x)$ across the two vertically stacked Au-SiO_2−Au nanocavities. Compared to NLNA, NLNOE benefits from the asymmetric geometry, and bottom nanohole arrays to support many hybridized plasmonic modes with high spatial mode overlaps over a broad wavelength range.[50,51]

Cyclic Voltammetry Modulation of Metal Luminescence from Plasmonic Hotspots. To investigate the effects of electrode potential modulation on PE-ERS and PE-VRS signals from plasmonic hotspots in NLNOEs, we performed *in situ* EC-SERS measurements of the NLNOE sample as the WE in 1× phosphate-buffered saline (PBS), using cyclic voltage sweep between −0.5 and 0.5 V at a voltage sweep rate of 50 mV/s with a saturated Ag/AgCl reference electrode. As shown in Figure 3A, top, the cyclic voltage sweep causes the periodic current modulations within ±0.2 mA associated with reversible non-Faradaic capacitive charging−discharging processes at the NLNOE surface.[52] The redox reaction between Au atoms and Cl^- ions at the electrode surface typically requires a higher positive potential (>1.5 V vs AgCl/Cl).[53] Figure 3A, bottom shows the time-dependent *in situ* EC-SERS spectra from −50 cm^{-1} to 500 cm^{-1}, where the dominant feature at ≈87 cm^{-1} is periodically modulated under cyclic voltage sweeping. Figure 3B illustrates five EC-SERS spectra recorded between −0.5 and 0.5 V in a half-cycle with several key observations. First, the small peak at ≈0 cm^{-1} accounts for the elastic scattering signal from the excitation laser (785 nm) leaking through the long-pass filter. Second, the asymmetric voltage-dependent spectral feature at ≈87 cm^{-1} is a PE-ERS pseudopeak due to the long-pass filter modification of the continuous Stokes ERS emission associated with the Bose−Einstein distribution of the metal sp-band electron−hole pairs at Stokes-shifted frequency $\Delta\omega$,[9,54,55] which decreases with the applied potential. Third, a PE-VRS shoulder feature at ≈270 cm^{-1} on top of the PE-ERS spectral background is from Au−Cl bonds formed on the gold surface,[56,57] which increases with the applied potential because of the attraction of the Cl^- ions to the gold surface under a positive potential.

Figure 3C compares the measured electrode potential dependence of the charging−discharging current and the emission modulation ratios ($\Delta I/I$) for PE-ERS, PE-VRS, and elastic scattering signals in a single cycle. First, by modeling the dominant non-Faradaic capacitive interfacial process with an equivalent circuit[58] consisting of a double-layer capacitor (C) and an ohmic resistance (R) in series, we can fit the measured current−potential (I−V) curve with $I = \frac{V}{R} + \frac{dV}{dt}C$ to estimate the capacitance of the NLNOE sample as $C \approx 1.8 \times 10^{-3}$ F (see details in Supporting Information). Second, the elastic scattering peak at ≈0 cm^{-1} has a negligible voltage modulation. Third, PE-VRS signals at ≈270 cm^{-1} from Au−Cl surface bonds have a positive linear dependence on potential changes on the positive voltage side. Interestingly, PE-VRS signals become less sensitive to electrode potential changes on the negative voltage side, suggesting the interfacial Au−Cl bond formation−deformation processes depend on the electrode potential polarities.[59] Fourth, the PE-ERS pseudopeak signal at ≈87 cm^{-1} shows a negative linear dependence on potential

https://doi.org/10.1021/acsnano.3c01491
ACS Nano 2023, 17, 8634−8645

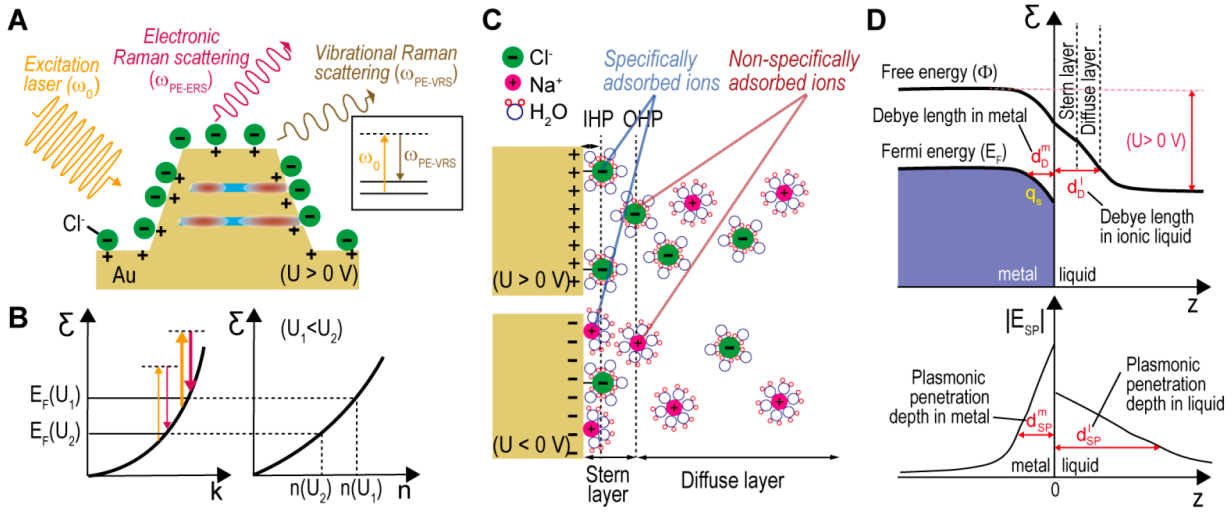

Figure 4. Mechanism for electrode potential modulation of PE-ERS signals from plasmonic hotspots at the metal−electrolyte interface. (A) The scheme of PE-ERS and PE-VRS light emission from plasmonic hotspots in the NLNOE with an applied electrode potential $U > 0$ V in the electrolyte. The inset shows the energy diagram of the VRS process. (B) The energy diagram scheme illustrates that the electrode penitential difference ($U_1 < U_2$) can change the ERS intensity by shifting the Fermi energy E_F and free electron density n at the metal surface. (C) The scheme of the local electrochemical environment at the electrode−electrolyte interface with positive (top) and negative (bottom) electrode surface potential U and induced surface charge. (D) The scheme of position-dependent energy distribution with a positive electrode potential ($U > 0$ V) (top) and surface plasmon electric field intensity $|E|^2$ profile (bottom) at the electrode−electrolyte interface.

changes with different voltage modulation slopes on the positive (≈30% V^{-1}) and the negative (≈15% V^{-1}) voltage sides, suggesting that interfacial charging−discharging processes also depend on the electrode potential polarities. The data shown in Figure 3C originates from a single cycle measurement (from 60 to 100 s). The reversibility of the system is verified through the modulation slope tracking, which can be found in Supporting Information, Figure S3. The coefficient of variations for positive and negative PE-ERS modulation slopes are 4.1% and 3.7%, respectively. Next, the broadband emission signal integrated from ≈600 cm^{-1} to ≈1200 cm^{-1} exhibits a negative linear voltage dependence with different voltage modulation rates on the positive (≈22% V^{-1}) and negative (≈18% V^{-1}) voltage sides, similar to the behaviors of the ERS pseudopeak signal at ≈87 cm^{-1}. Last, the voltage-modulation slopes for both PE-VRS and PE-ERS signals change around ≈0 V, manifesting that the Au surface in 1× PBS with pH of ≈7.4 has a point of zero charge (PZC) potential U_{PZC} around ≈0 V in our measurements, which is reasonable as previous work shows with similar polycrystalline gold substrate.[60]

Modeling of Electrode Potential-Modulated Plasmonic Metal Luminescence in Electrolytes. To understand the voltage modulation behaviors for PE-ERS and PE-VRS signals from NLNOEs, we need to consider optical, electronic, and ionic activities in the plasmonic hotspots at the metal−electrolyte interface. As illustrated in Figure 4A, the laser excitation of plasmonic modes in NLNOEs can concentrate intense optical fields in multinanogap MIM nanocavities[61] to generate PE-VRS signals from Au−Cl surface bonds and PE-ERS signals from Au sp-band electron−hole pairs. Like PE-VRS, surface plasmon modes can simultaneously enhance excitation (ω_0) and emission (ω) transitions for PE-ERS to realize a significant enhancement factor $F(\omega_0,\omega,\boldsymbol{r}) \approx |E_{SP}(\omega_0,\boldsymbol{r})|^2 \cdot |E_{SP}(\omega,\boldsymbol{r})|^2 \approx |E_{SP}(\omega_0,\boldsymbol{r})|^4$, where $|E_{SP}|$ is the local electric field amplitude at position $\boldsymbol{r}$ inside the metal. In this way, we can express the PE-ERS flux density as,

$$i_{PE\text{-}ERS}(\omega_0, \omega, \boldsymbol{r}) \approx F(\boldsymbol{r})\cdot i_{in}(\omega_0)\cdot\sigma_{ERS}(\omega_0, \omega)\cdot |e^{-\hbar(\omega_0-\omega)/k_BT} - 1|^{-1}\cdot n(\boldsymbol{r}) = F(\boldsymbol{r})\cdot K\cdot n(\boldsymbol{r}) \quad (1)$$

where i_{in} is the incident laser flux density, σ_{ERS} is the cross section coefficient for an ERS event, $|e^{-\hbar(\omega_0-\omega)/k_BT} - 1|^{-1}$ is the Bose−Einstein distribution of the electron−hole pairs at Stokes-shifted frequency $\Delta\omega = \omega_0 - \omega$, and $n(\boldsymbol{r})$ is the local free electron density in the metal. By defining $K = i_{in}(\omega_0)\cdot\sigma_{ERS}(\omega_0, \omega)\cdot|e^{-\hbar(\omega_0-\omega)/k_BT} - 1|^{-1}$, the PE-ERS flux density becomes a position-dependent function as $i_{PE-ERS} = F(\boldsymbol{r})\cdot K\cdot n(\boldsymbol{r})$.[54] Because $n(\boldsymbol{r})$ directly couples with the local Fermi energy level as $E_F(\boldsymbol{r}) = \frac{\hbar^2}{2m}[3\pi^2 n(\boldsymbol{r})]^{2/3}$, the change of electrode potential U at the electrolyte interface can modulate $E_F(\boldsymbol{r})$ and accordingly $n(\boldsymbol{r})$ within the Debye length d_D^m (≈0.15 nm for Au) at the metal surface.[62,63] Thus, as illustrated in Figure 4A,B, the electrode potential modulation ($U_1 < U_2$) can change PE-ERS intensity from the hotspots in which the metal is electrically connected to the working electrode substrate and exposed to the electrolyte.

Figure 4C illustrates that the change between positive and negative electrode potentials will reverse the electrical polarities of induced metal surface charges and ionic species in the electrical double layer (EDL) at the electrode−electrolyte interface. As a general model, the EDL structure consists of (i) the Stern layer with the inner Helmholtz plane (IHP) for specifically adsorbed ions and the outer Helmholtz plane (OHP) for nonspecifically adsorbed ions and (ii) the diffuse layer for free-moving ions. Under $U > 0$ V, the positively charged metal surface can electrostatically attract negatively charged ions to increase the surface density of both specifically and nonspecifically adsorbed Cl^- ions in the Stern layer.[57,64] The increased surface density of specifically adsorbed Cl^- ions under positive potential can lead to more noncovalent Au−Cl surface bonds at the Au surface. On the

https://doi.org/10.1021/acsnano.3c01491
ACS Nano 2023, 17, 8634−8645

other hand, applying negative electrode potentials (e.g., $U < -0.5$ V) will increase the number of specifically and nonspecifically adsorbed positive ions (e.g., Na^+) and deplete the noncovalent Au−Cl surface bonds, while those more stable covalent Au−Cl surface bonds can remain. Such a scheme can explain the observation in Figure 3C that PE-VRS signals at ≈270 cm^{-1} show a positive modulation rate on positive voltages by forming noncovalent Au−Cl surface bonds but an insensitive modulation on negative voltages due to the depletion of noncovalent Au−Cl surface bonds. Furthermore, because Cl^- and Na^+ ions have different electric susceptibility values, the polarity change of electrode potential can modulate the local dielectric permittivity ϵ_D^l in EDL environment by switching the types of ionic species which occupy the Stern layer, which will further affect the voltage modulation rates for PE-ERS signals, as discussed later.

As illustrated in Figure 4D, top, applying a positive electrode potential ($U > 0$ V) can drastically distort the electronic free energy $\Phi(z)$ across the interfacial region of the metal Debye length d_D^m (≈ 0.15 nm for Au) and the electrolyte Debye length d_D^l (≈ 0.79 nm for 1× PBS, ionic strength: ≈0.15 mol/L). Accordingly, local Fermi energy $E_F(z)$ and local free electron density $n(z)$ can be electrically modulated within d_D^m at the metal surface. It should be noted here that $E_F(z)$ may also be modulated due to the adsorbed halide ions.[65] As the slope of PE-ERS vs potential nearly does not alter over sequential cycles (Supporting Information, Figure 3), the potential influence on PE-ERS from the accumulation of covalently bonded chloride ions can be ruled out. In contrast, Figure 4D, bottom shows that the local electric field amplitude $|E_{SP}|$ for the surface plasmon mode exponentially decreases from the metal−liquid interface with the characteristic penetration lengths d_{SP}^m and d_{SP}^l on the metal and electrolyte sides. In this experiment, d_{SP}^m can be approximated as ≈5 nm according to the mode confinement dimension for the surface plasmons supported in the MIM nanocavity.[66] As a first-order approximation, we can express the z-dependent PE-ERS enhancement factor as

$$F(z) \approx |E_{SP}(z)|^4 \approx |E_{SP}(z=0)|^4 \cdot e^{-4z/d_{SP}^m} = F_{max} \cdot e^{-4z/d_{SP}^m} \tag{2}$$

Using eqs 1 and eq 2, we can express the total PE-ERS flux from a plasmonic nanocavity hotspot with a mode surface area A_{tot} as

$$\begin{aligned} I_{PE\text{-}ERS} &\approx \int_0^\infty i_{PE\text{-}ERS}(z) \cdot A_{tot} \cdot dz \\ &\approx K \cdot F_{max} \cdot A_{tot} \cdot \int_0^\infty n(z) \cdot e^{-4z/d_{SP}^m} \cdot dz \end{aligned} \tag{3}$$

In the condition with a zero electrode surface potential ($U_0 \approx U_{PZC} \approx 0$ V), the free electron density $n(z) = n(U_0)$ is uniform inside the metal, and we can use eqs 2−3 to express the PE-ERS flux as

$$\begin{aligned} I_{PE\text{-}ERS}(U_0) &\approx K \cdot F_{max} \cdot A_{tot} \cdot n(U_0) \cdot \int_0^\infty e^{-4z/d_{SP}^m} \cdot dz \\ &= \frac{1}{4} \cdot K \cdot F_{max} \cdot A_{tot} \cdot n(U_0) \cdot d_{SP}^m \end{aligned} \tag{4}$$

On the other side, with a nonzero electrode potential ($U \neq 0$ V), we can decompose the plasmonic hotspot mode surface into (i) the region exposed to the electrolyte with an area of A_{exp}, and (ii) the embedded region with an area of $A_{tot} - A_{exp}$. Within the electrolyte-exposed hotspot region under electrode potential U, we can approximate the z-dependent free electron density profile $n(z)$ as (i) $n(U)$ within the metal Debye length $|z| < d_D^m$, and (ii) $n(U_0)$ outside the metal Debye length $|z| > d_D^m$. By defining a local EDL capacitance at the plasmonic hotspot as

$$C^* \approx \frac{\epsilon_D^l}{d_D^l} \cdot A_{exp} \tag{5}$$

we can express the free electron density change with electrode potential modulation within the metal Debye length as

$$\Delta n = n(U) - n(U_0) \approx \frac{C^* \cdot (U - U_0)}{-e \cdot A_{exp} \cdot d_D^m} \approx \frac{(U - U_0)}{-e \cdot d_D^m} \cdot \frac{\epsilon_D^l}{d_D^l} \tag{6}$$

Using eqs 4−6, we can model the potential modulated PE-ERS flux from a hotspot as

$$\begin{aligned} \Delta I_{PE\text{-}ERS} &= I_{PE\text{-}ERS}(U) - I_{PE\text{-}ERS}(U_0) \approx K \cdot F_{max} \cdot A_{exp} \cdot \\ &\int_0^{d_D^m} [n(U) - n(U_0)] \cdot e^{-4z/d_{SP}^m} \cdot dz \approx K \cdot F_{max} \cdot A_{exp} \cdot \\ &[n(U) - n(U_0)] \cdot d_D^m \approx K \cdot F_{max} \cdot \frac{C^* \cdot (U - U_0)}{-e} \\ &\approx K \cdot F_{max} \cdot \frac{(U - U_0) \cdot A_{exp}}{-e} \cdot \frac{\epsilon_D^l}{d_D^l} \end{aligned} \tag{7}$$

Using eqs 4 and 7, the modulation ratio for PE-ERS flux from a hotspot can be expressed as

$$\begin{aligned} \frac{\Delta I_{PE\text{-}ERS}}{I_{PE\text{-}ERS}(U_0)} &\approx -\frac{4 \cdot (U - U_0)}{n(U_0) \cdot e} \cdot \frac{1}{d_{SP}^m} \cdot \frac{C^*}{A_{tot}} \\ &\approx -\frac{4 \cdot (U - U_0)}{n(U_0) \cdot e} \cdot \frac{\epsilon_D^l}{d_D^l} \cdot \frac{1}{d_{SP}^m} \cdot \frac{A_{exp}}{A_{tot}} \end{aligned} \tag{8}$$

Our analytical model in eq 8 can reasonably agree with the observations in Figure 3C. First, the PE-ERS signal modulation ratio $\frac{\Delta I_{PE\text{-}ERS}(\Delta U)}{I_{PE\text{-}ERS}(U_0)}$ has a negative linear dependence on the electrode potential U, considering $U_0 \approx U_{PZC} \approx 0$ V in our measurements. Second, the potential modulation slope $\frac{\Delta I_{PE\text{-}ERS}(\Delta U)}{I_{PE\text{-}ERS}(U_0)}$ depends on the local dielectric permittivity ϵ_D^l in the EDL and thus can change values by switching polarities of electrode surface potential and ionic species with different susceptibilities in the Stern layer.[53]

Ion Concentration Effects on Voltage Modulation of Plasmonic Metal Luminescence. Significantly, eq 8 predicts that the PE-ERS voltage modulation rate $\frac{\Delta I_{PE\text{-}ERS}(\Delta U)}{\Delta U \cdot I_{PE\text{-}ERS}(U_0)}$ is proportional to the local capacitance $C^* \approx \frac{\epsilon_D^l}{d_D^l} \cdot A_{exp}$ at the electrolyte-exposed plasmonic hotspot region and thus depends on the local electrolyte capacitive characteristics in $\frac{\epsilon_D^l}{d_D^l}$. Because increasing ion concentration P in the electrolyte can decrease d_D^l and increase ϵ_D^l, we expect that $\frac{\Delta I_{PE\text{-}ERS}(\Delta U)}{\Delta U \cdot I_{PE\text{-}ERS}(U_0)}$ can increase with ion concentration P due to increased C^*. To validate this model prediction, we conducted experiments to measure the electrode potential U-dependent $\frac{\Delta I_{PE\text{-}ERS}(\Delta U)}{I_{PE\text{-}ERS}(U_0)}$ in

https://doi.org/10.1021/acsnano.3c01491
ACS Nano 2023, 17, 8634−8645

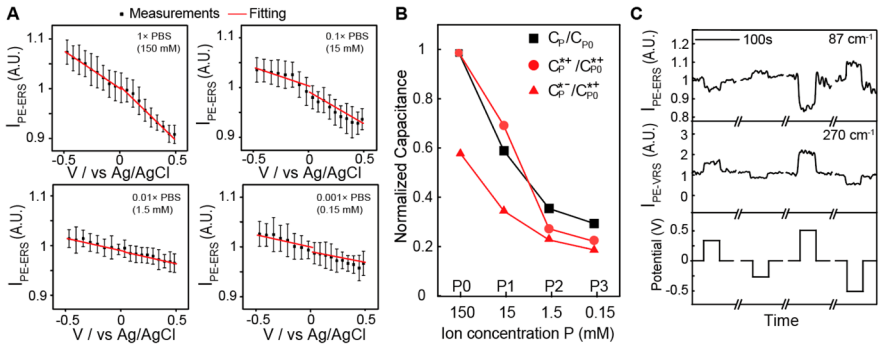

Figure 5. Ion concentration dependence and dynamic responses of electrode potential modulated PE-ERS signals in the electrolyte. (A) The measured and fitted PE-ERS intensities from NLNOEs as a function of electrode potentials in the electrolyte with different ion concentrations. Each data point represents the average amount of the $\frac{\Delta I}{I}$ at a specific voltage among the total 5 cycles, and the error bars represent the standard deviation among the 5 cycles. (B) The normalized macroscopic capacitance C_P/C_{P0} and microscopic capacitance $C_P^{*,+}/C_{P0}^{*,+}$ ($U > 0$ V) and $C_P^{*,-}/C_{P0}^{*,+}$ ($U < 0$ V) for the electrical double layer (EDL) at different ion concentrations by fitting the measurements in cyclic potential-dependent currents and PE-ERS signals, respectively. (C) Time-resolved PE-ERS traces at ≈87 cm^{-1}, and PE-VRS traces at ≈270 cm^{-1} from NLNOEs in 1× PBS under electrode potential modulation of square wave functions.

electrolytes with different ion concentrations P, including 1× PBS (P0 = 150 mol/m^3), diluted 0.1× PBS (P1 = 15 mol/m^3), diluted 0.01× PBS (P2 = 1.5 mol/m^3), and diluted 0.001× PBS (P3 = 0.15 mol/m^3) solutions. Figure 5A shows the experimental U vs $\frac{\Delta I_{PE\text{-}ERS}(\Delta U)}{I_{PE\text{-}ERS}(U_0)}$ results from *in situ* EC-SERS measurements of NLNOEs in electrolytes of different P under cyclic voltage sweeping between −0.5 and 0.5 V at a ≈50 mV/s scan rate for five cycles. There are several observations. First, $\frac{\Delta I_{PE\text{-}ERS}(\Delta U)}{I_{PE\text{-}ERS}(U_0)}$ has a negative linear dependence on U but with a reduced slope amplitude at lower ion concentrations P. Second, in higher ion concentration electrolytes (150 mol/m^3 and 15 mol/m^3), the PE-ERS voltage modulation slope amplitude is higher in positive than negative electrode potentials, while the slope difference significantly drops in lower ion concentration electrolytes (1.5 mol/m^3 and 0.15 mol/m^3).

By defining a slope coefficient as $b_P^{*,\pm} = \frac{4}{n(U_0)\cdot e}\cdot\frac{1}{d_{sp}^m}\cdot\frac{C_P^{*,\pm}}{A_{tot}}$ at positive (+) and negative (−) electrode potentials, we can express eq 8 as

$$\frac{\Delta I_P(U)}{I_P(U_0)} \approx -b_P^{*,\pm}\cdot(U - U_0) \tag{9}$$

to fit measurements as red lines in Figure 5A and extract the fitted $b_P^{*,\pm}$ slope coefficients at different ion concentrations P and electrode polarities (±). Based on $b_P^{*,\pm}/b_{P0}^{*,+} = C_P^{*,\pm}/C_{P0}^{*,+}$ in a ratiometric normalization with the P_0 values from 1× PBS, Figure 5B quantitively illustrates the effects of ion concentrations P and electrode potential polarities (±) on the PE-ERS retrieved local capacitance values $C_P^{*,\pm}/C_{P0}^{*,+}$ from nanoscale plasmonic hotspots, which reveals several crucial points by comparing with the cyclic I–V extracted macroscopic capacitance C_P/C_{P0} from the cm^2 scale NLNOE sample area. First, both macroscopic capacitance C_P/C_{P0} and microscopic capacitance $C_P^{*,\pm}/C_{P0}^{*,+}$ values decrease with decreasing P, manifesting that $\frac{\epsilon_D^l}{d_D^l}$ of the electrolyte EDL depends on ion concentration P. Second, the observation of much-increased differences between $C_P^{*,+}/C_{P0}^{*,+}$ and $C_P^{*,-}/C_{P0}^{*,+}$ only at higher ion concentrations suggest that a short electrolyte Debye length d_D^l (e.g., ≈ 0.79 nm for 150 mol/m^3, ≈ 2.5 nm for for 15 mol/m^3) may cause a more significant effect of the difference in electric susceptibility and, accordingly, dielectric permittivity between specifically/nonspecifically adsorbed Cl^- and Na^+ species within the Stern layer under opposite U polarities on local capacitance values at hotspots.[67,68] Overall, the agreement between the experimental data and the fitting results with different ion concentrations substantiates the credibility of the developed model.

As shown in Figure 5C, we measured the temporal responses of the PE-ERS pseudo peak at ≈87 cm^{-1} and Au−Cl PE-VRS peak at ≈270 cm^{-1} under voltage square waves alternating at ±0.3 V, 0 V, or ±0.5 V in 1× PBS with an integration time of 0.5 s. Similar to measurements under cyclic sweeping conditions in Figure 3C, the square-wave inputs produce more significant voltage modulation of the PE-ERS and PE-VRS signals under the positive ($U > 0$ V) than negative electrode potentials ($U < 0$ V) with similar voltage modulation rates, manifesting that the underlying electrode potential modulation mechanisms for PE-ERS and PE-VRS signals remain the same under different input voltage shapes.

Significantly, our measurements in Figure 3C and Figure 5C demonstrate that biocompatible Au-based NLNOEs can produce PE-ERS signals with a substantial voltage modulation rate $\frac{\Delta I_{PE\text{-}ERS}(\Delta U)}{\Delta U\cdot I_{PE\text{-}ERS}(U_0)}$ of ≈15% V^{-1} to ≈30% V^{-1} in physiological electrolytes (e.g., 1× PBS); thus, they can potentially serve as label-free nonlinear voltage nanosensors. Although the PE-ERS voltage modulation rate from NLNOEs is still lower than label-based voltage-sensitive fluorophores (80% to 200% V^{-1})[69] and recently reported label-free linear scattering-based voltage nanotransducers (≈100% V^{-1}),[70,71] they may enjoy advantage by combining label-free operations, low phototoxicity, excellent photostability, and nonlinear NIR deep-tissue sensing/imaging modalities by filtering elastic scattering background. Furthermore, our analytical model in eqs 7 and 8 reveals that there is room to improve the PE-ERS voltage modulation performance in signal brightness and voltage sensitivity. To enhance the PE-ERS voltage modulation amplitude $\frac{\Delta I_{PE\text{-}ERS}(\Delta U)}{\Delta U}$, that is the signal brightness, we can (i) increase the PE-ERS enhancement factor $F_{max} \approx |E_{SP}(z = 0)|^4$ by optimizing near-field plasmonic characteristics and (ii)

https://doi.org/10.1021/acsnano.3c01491
ACS Nano 2023, 17, 8634−8645

expand the electrolyte-exposed mode area A_{exp} at the hotspot by engineering nanocavity geometries. On the other hand, achieving a higher PE-ERS voltage modulation rate $\frac{\Delta I_{PE\text{-}ERS}(\Delta U)}{\Delta U \cdot I_{PE\text{-}ERS}(U_0)}$, that is the signal voltage sensitivity, requires (i) reducing the penetration depth d_{SP}^m in the metal at the hotspot by optimizing near-field plasmonic characteristics, and (ii) increasing the exposed area ratio $\frac{A_{exp}}{A_{tot}}$ by engineering nanocavity geometries.

Finally, we note that the PE-ERS signals possess much higher voltage modulation sensitivity than the traditional elastic scattering-based plasmonic devices[72] because the tightly confined voltage-induced surface electron density changes within the metal Debye length d_D^m (≈0.15 nm) have a high spatial overlap with the plasmonic enhancement profile $|E_{SP}|^4 \cdot e^{-4z/d_{SP}^m}$ for PE-ERS signals with a tight $|E_{SP}|^4$ -related optical depth in the metal of $\frac{d_{SP}^m}{4}$. Meanwhile, for the elastic channel, the resonance wavelength shifts, or intensity changes are determined by the total bulk charge density changes of the plasmonic resonator,[72] causing weaker voltage modulation rates.

CONCLUSION

In conclusion, we have demonstrated a substantial capacitive voltage modulation (up to ≈30% V^{-1}) of nanoplasmonic metal luminescence associated with PE-ERS signals from hotspots at the electrode−electrolyte interface using multiresonant NLNOE arrays. We have developed a simple phenomenological model to capture critical plasmonic, electronic, and ionic characteristics at the metal−electrolyte interface to understand experimental observations, which can also provide guidelines for further performance improvement. Significantly, this study reveals that the voltage modulation of PE-ERS metal luminescence signals originates from the spatial overlap between the plasmonic mode $|E_{SP}|^4$ penetration depth $\frac{d_{SP}^m}{4}$ and electronic Debye length d_D^m for the electrolyte-exposed metal surface at hotspots and can follow the changes in microscopic capacitive characteristics (e.g., local electrolyte Debye length d_D^l, local dielectric permittivity ϵ_D^l) at the electrode−electrolyte interface. While this study primarily concentrates on modeling and analyzing PE-ERS originating from Au-based MIM nanocavity hotspots under NIR laser excitation, the developed model can be extended to include other potential plasmon-enhanced metal luminescence processes, such as intraband and interband photoluminescence of hot carriers within the metal. This generalization is feasible because these plasmon-enhanced metal luminescence mechanisms involve plasmonic near-field enhancements and the transition of electrons near the Fermi level. While additional work will be needed, for example, to improve signal brightness and voltage sensitivity by optimizing nano-optoelectrode designs, the current work represents a critical step toward the general application of nanoplasmonic metal luminescence in optical voltage biosensing, hybrid optical−electrical signal transduction, and interfacial monitoring of electrochemical processes.

METHODS

Fabrication of Nano-Optode Arrays. First, a reusable PFPE nanopillar array template on a PET substrate was created from a silicon master of square nanowell (diameter ≈120 nm, depth ≈300 nm, and periodicity ≈400 nm) arrays using nanoimprint lithography. Next, the PFPE nanopillar array was spin-coated with diluted PMMA solution, and the PMMA nanowell arrays were transferred onto an ITO-coated glass slide using thermal nanoimprinting (∼100 °C, 12 h). The PMMA nanowells were then transformed into nanoholes using RIE, forming a deposition mask for e-beam evaporation of alternating Au (≈25 nm) and SiO_2 (≈10 nm) thin-film layers. Subsequently, the PMMA was dissolved in anisole, removing excess material and revealing an array of NLNAs with MIM nanocavities. Lastly, a ≈30 nm thick Au layer was coated on NLNAs with a tilted angle (≈50°) for the substrate. The NLNOE is achieved after the off-angle deposition of the Au layer.

Reflectance and Transmittance Measurements. Samples' reflectance and transmittance spectra were measured by a UV−vis−near-infrared (NIR) spectrophotometer (Cary 5000). The wavelength range is from 400 to 900 nm with the step 0.5 nm.

Numerical Silations. The 3D FDTD simulations were performed by commercial software (FDTD solutions, Ansys-Lumerical Inc.) to numerically calculate the far-field spectra and the near-field distributions of the plasmonic systems. Optical constants of Au were taken from Johnson and Christy[73] in the spectrum range from 400 to 900 nm, and n = 1.5 was used for SiO_2. A mesh with a resolution of 1 nm in x, y, and z directions was used for the NLNOE. To mimic the geometry of the nanolaminate SERS substrate according to the SEM and FIB images, we construct the square lattice with 400 nm periodic boundary conditions in the x−y plane. For the noncoated and coated nanopillar structure, we adopted a trapezoidal multilayered nanopillar and a coating layer diagonally oriented in the square lattice.

Electrochemical Measurements. A custom-made EC cell was constructed to contain the liquid and mounted onto the sample. An Ag/AgCl electrode saturated in KCl served as the reference electrode, while a platinum coil functioned as the counter electrode. Phosphate buffer saline (PBS) was employed as the electrolyte solution, consisting of 137 mM NaCl, 2.7 mM KCl, 10 mM Na_2HPO_4, and 1.8 mM KH_2PO_4. Deionized water was used for the dilution of the PBS. Approximately 2 mL of the electrolyte solution was introduced into the EC cell, and measurements were conducted at room temperature. To prevent electrolyte purging issues over an extended time scale (hours), we carried out all measurements within approximately 10 min immediately following the addition of the liquid. For all measurements, the substrate was rinsed with the corresponding concentration of PBS solution between each use to ensure cleanliness and reliability.

EC-SERS Measurements. Raman measurements were done under laser excitation at a wavelength of 785 nm and power of 2 mW *via* a 10× objective (NA = 0.25) lens with a commercial confocal microscope in the backscattering configuration. Single-point measurements were done at a 0.5 s integration time and acquired by a CCD camera in a commercial spectrometer to measure the Stokes−Raman scattering. A long-pass filter was used to block elastically scattered light at the wavelength corresponding to the laser line (Rayleigh scattering), and the Stokes scattering passed through a multimode fiber (100 μm core diameter) with the cleaved fiber core acting as the confocal pinhole. EC modulation was done using a custom EC cell and commercial potentiostat with the NLNOE as the working electrode, platinum coil as the counter electrode, and Ag/AgCl as the reference electrode.

ASSOCIATED CONTENT

Supporting Information

The Supporting Information is available free of charge at https://pubs.acs.org/doi/10.1021/acsnano.3c01491.

Plasmonic mode analysis at 610 nm under under ∥ and ⊥ polarized illumination (PDF)

https://doi.org/10.1021/acsnano.3c01491
ACS Nano 2023, 17, 8634−8645

AUTHOR INFORMATION

Corresponding Author

Wei Zhou − *Department of Electrical and Computer Engineering, Virginia Tech, Blacksburg, Virginia 24061, United States;* orcid.org/0000-0002-5257-3885; Email: wzh@vt.edu

Authors

Yuming Zhao − *Department of Electrical and Computer Engineering, Virginia Tech, Blacksburg, Virginia 24061, United States*

Chuan Xiao − *Department of Electrical and Computer Engineering, Virginia Tech, Blacksburg, Virginia 24061, United States*

Elieser Mejia − *Department of Electrical and Computer Engineering, Virginia Tech, Blacksburg, Virginia 24061, United States*

Aditya Garg − *Department of Electrical and Computer Engineering, Virginia Tech, Blacksburg, Virginia 24061, United States*

Junyeob Song − *Physical Measurement Laboratory, National Institute of Standards and Technology, Gaithersburg, Maryland 20899, United States*

Amit Agrawal − *Physical Measurement Laboratory, National Institute of Standards and Technology, Gaithersburg, Maryland 20899, United States;* orcid.org/0000-0002-9619-7623

Complete contact information is available at: https://pubs.acs.org/10.1021/acsnano.3c01491

Author Contributions

Y.Z. and W.Z. conceived the idea. W. Z. supervised the project. Y.Z. performed optical measurements, numerical simulations, and the corresponding data analysis with the help of W.Z. and E.M. Y.Z. and C.X. performed electrochemical measurements. Samples were fabricated collectively by Y.Z., C.X, E.M., A.G, and J.S. contributed to structural characterization by FIB/SEM. A.A. contributed to discussing and commenting on the manuscript. Y.Z. and W.Z. wrote the manuscript with the contributions of all authors. All authors have approved the final version of the manuscript.

Notes

The authors declare no competing financial interest.

ACKNOWLEDGMENTS

This work was supported by AFOSR Young Investigator Award FA9550-18-1-0328, US NSF grant DMR2139317, US AFOSR DURIP Award FA9550-19-1-0287, US NIST grant 70NANB18H201, and US NIST grant 70NANB19H163

REFERENCES

(1) Pelton, M. Modified spontaneous emission in nanophotonic structures. *Nat. Photonics* **2015**, *9* (7), 427−435.

(2) Sun, G.; Khurgin, J. B. Origin of giant difference between fluorescence, resonance, and nonresonance Raman scattering enhancement by surface plasmons. *Phys. Rev. A* **2012**, *85*, 063410.

(3) Kauranen, M.; Zayats, A. V. Nonlinear plasmonics. *Nat. Photonics* **2012**, *6* (11), 737−748.

(4) Zhou, W.; Dridi, M.; Suh, J. Y.; Kim, C. H.; Co, D. T.; Wasielewski, M. R.; Schatz, G. C.; Odom, T. W. Lasing action in strongly coupled plasmonic nanocavity arrays. *Nat. Nanotechnol.* **2013**, *8* (7), 506−511.

(5) Kinkhabwala, A.; Yu, Z. F.; Fan, S. H.; Avlasevich, Y.; Mullen, K.; Moerner, W. E. Large single-molecule fluorescence enhancements produced by a bowtie nanoantenna. *Nat. Photonics* **2009**, *3* (11), 654−657.

(6) Celebrano, M.; Wu, X. F.; Baselli, M.; Grossmann, S.; Biagioni, P.; Locatelli, A.; De Angelis, C.; Cerullo, G.; Osellame, R.; Hecht, B.; Duo, L.; Ciccacci, F.; Finazzi, M. Mode matching in multiresonant plasmonic nanoantennas for enhanced second harmonic generation. *Nat. Nanotechnol.* **2015**, *10* (5), 412−417.

(7) Aouani, H.; Rahmani, M.; Navarro-Cia, M.; Maier, S. A. Third-harmonic-upconversion enhancement from a single semiconductor nanoparticle coupled to a plasmonic antenna. *Nat. Nanotechnol.* **2014**, *9* (4), 290−294.

(8) Zong, C.; Xu, M.; Xu, L. J.; Wei, T.; Ma, X.; Zheng, X. S.; Hu, R.; Ren, B. Surface-Enhanced Raman Spectroscopy for Bioanalysis: Reliability and Challenges. *Chem. Rev.* **2018**, *118* (10), 4946−4980.

(9) Hugall, J. T.; Baumberg, J. J. Demonstrating Photoluminescence from Au is Electronic Inelastic Light Scattering of a Plasmonic Metal: The Origin of SERS Backgrounds. *Nano Lett.* **2015**, *15* (4), 2600−2604.

(10) Mahajan, S.; Cole, R. M.; Speed, J. D.; Pelfrey, S. H.; Russell, A. E.; Bartlett, P. N.; Barnett, S. M.; Baumberg, J. J. Understanding the Surface-Enhanced Raman Spectroscopy "Background". *J. Phys. Chem. C* **2010**, *114* (16), 7242−7250.

(11) Sivan, Y.; Dubi, Y. Theory of "Hot" Photoluminescence from Drude Metals. *ACS Nano* **2021**, *15* (5), 8724−8732.

(12) Cai, Y. Y.; Tauzin, L. J.; Ostovar, B.; Lee, S.; Link, S. Light emission from plasmonic nanostructures. *J. Chem. Phys.* **2021**, *155* (6), 060901.

(13) Carattino, A.; Caldarola, M.; Orrit, M. Gold Nanoparticles as Absolute Nanothermometers. *Nano Lett.* **2018**, *18* (2), 874−880.

(14) Xie, X.; Cahill, D. G. Thermometry of plasmonic nanostructures by anti-Stokes electronic Raman scattering. *Appl. Phys. Lett.* **2016**, *109*, 183104.

(15) Zheng, Z. K.; Tachikawa, T.; Majima, T. Single-Particle Study of Pt-Modified Au Nanorods for Plasmon-Enhanced Hydrogen Generation in Visible to Near-Infrared Region. *J. Am. Chem. Soc.* **2014**, *136* (19), 6870−6873.

(16) Durr, N. J.; Larson, T.; Smith, D. K.; Korgel, B. A.; Sokolov, K.; Ben-Yakar, A. Two-photon luminescence imaging of cancer cells using molecularly targeted gold nanorods. *Nano Lett.* **2007**, *7* (4), 941−945.

(17) Zheng, Z. K.; Majima, T. Nanoplasmonic Photoluminescence Spectroscopy at Single-Particle Level: Sensing for Ethanol Oxidation. *Angew. Chem. Int. Edit* **2016**, *55* (8), 2879−2883.

(18) Boyd, G. T.; Yu, Z. H.; Shen, Y. R. Photoinduced Luminescence from the Noble-Metals and Its Enhancement on Roughened Surfaces. *Phys. Rev. B* **1986**, *33* (12), 7923−7936.

(19) Mooradian, A. Photoluminescence of Metals. *Phys. Rev. Lett.* **1969**, *22*, 185.

(20) Beversluis, M. R.; Bouhelier, A.; Novotny, L. Continuum generation from single gold nanostructures through near-field mediated intraband transitions. *Phys. Rev. B* **2003**, *68*, 115433.

(21) Ostovar, B.; Cai, Y. Y.; Tauzin, L. J.; Lee, S. A.; Ahmadivand, A.; Zhang, R.; Nordlander, P.; Link, S. Increased Intraband Transitions in Smaller Gold Nanorods Enhance Light Emission. *ACS Nano* **2020**, *14* (11), 15757−15765.

(22) Cai, Y. Y.; Liu, J. G.; Tauzin, L. J.; Huang, D.; Sung, E.; Zhang, H.; Joplin, A.; Chang, W. S.; Nordlander, P.; Link, S. Photoluminescence of Gold Nanorods: Purcell Effect Enhanced Emission from Hot Carriers. *ACS Nano* **2018**, *12* (2), 976−985.

(23) Lin, K.-Q.; Yi, J.; Hu, S.; Sun, J.-J.; Zheng, J.-T.; Wang, X.; Ren, B. Intraband hot-electron photoluminescence from single silver nanorods. *Acs Photonics* **2016**, *3* (7), 1248−1255.

(24) Mertens, J.; Kleemann, M. E.; Chikkaraddy, R.; Narang, P.; Baumberg, J. J. How Light Is Emitted by Plasmonic Metals. *Nano Lett.* **2017**, *17* (4), 2568−2574.

(25) Huang, J.; Wang, W.; Murphy, C. J.; Cahill, D. G. Resonant secondary light emission from plasmonic Au nanostructures at high

electron temperatures created by pulsed-laser excitation. *Proc. Natl. Acad. Sci. U. S. A.* **2014**, *111* (3), 906−911.
(26) Nam, W.; Zhao, Y. M.; Song, J.; Ali Safiabadi Tali, S.; Kang, S. J.; Zhu, W. Q.; Lezec, H. J.; Agrawal, A.; Vikesland, P. J.; Zhou, W. Plasmonic Electronic Raman Scattering as Internal Standard for Spatial and Temporal Calibration in Quantitative Surface-Enhanced Raman Spectroscopy. *J. Phys. Chem. Lett.* **2020**, *11*, 9543−9551.
(27) Carles, R.; Bayle, M.; Benzo, P.; Benassayag, G.; Bonafos, C.; Cacciato, G.; Privitera, V. Plasmon-resonant Raman spectroscopy in metallic nanoparticles: Surface-enhanced scattering by electronic excitations. *Phys. Rev. B* **2015**, *92*, 174302.
(28) Cai, Y. Y.; Sung, E.; Zhang, R.; Tauzin, L. J.; Liu, J. G.; Ostovar, B.; Zhang, Y.; Chang, W. S.; Nordlander, P.; Link, S. Anti-Stokes Emission from Hot Carriers in Gold Nanorods. *Nano Lett.* **2019**, *19* (2), 1067−1073.
(29) Roloff, L.; Klemm, P.; Gronwald, I.; Huber, R.; Lupton, J. M.; Bange, S. Light Emission from Gold Nanoparticles under Ultrafast Near-Infrared Excitation: Thermal Radiation, Inelastic Light Scattering, or Multiphoton Luminescence? *Nano Lett.* **2017**, *17* (12), 7914−7919.
(30) Lin, K. Q.; Yi, J.; Zhong, J. H.; Hu, S.; Liu, B. J.; Liu, J. Y.; Zong, C.; Lei, Z. C.; Wang, X.; Aizpurua, J. Plasmonic photoluminescence for recovering native chemical information from surface-enhanced Raman scattering. *Nat. Commun.* **2017**, *8*, 14891.
(31) Willets, K. A. Probing nanoscale interfaces with electrochemical surface-enhanced Raman scattering. *Curr. Opin Electroche* **2019**, *13*, 18−24.
(32) Wu, D. Y.; Li, J. F.; Ren, B.; Tian, Z. Q. Electrochemical surface-enhanced Raman spectroscopy of nanostructures. *Chem. Soc. Rev.* **2008**, *37* (5), 1025−1041.
(33) Tian, Z. Q.; Ren, B. Adsorption and reaction at electrochemical interfaces as probed by surface-enhanced Raman spectroscopy. *Annu. Rev. Phys. Chem.* **2004**, *55*, 197−229.
(34) Di Martino, G.; Turek, V. A.; Lombardi, A.; Szabo, I.; de Nijs, B.; Kuhn, A.; Rosta, E.; Baumberg, J. J. Tracking Nanoelectrochemistry Using Individual Plasmonic Nanocavities. *Nano Lett.* **2017**, *17* (8), 4840−4845.
(35) Wilson, A. J.; Molina, N. Y.; Willets, K. A. Modification of the Electrochemical Properties of Nile Blue through Covalent Attachment to Gold As Revealed by Electrochemistry and SERS. *J. Phys. Chem. C* **2016**, *120* (37), 21091−21098.
(36) Shegai, T.; Vaskevich, A.; Rubinstein, I.; Haran, G. Raman Spectroelectrochemistry of Molecules within Individual Electromagnetic Hot Spots. *J. Am. Chem. Soc.* **2009**, *131* (40), 14390−14398.
(37) Do, H.; Kwon, S. R.; Fu, K. Y.; Morales-Soto, N.; Shrout, J. D.; Bohn, P. W. Electrochemical Surface-Enhanced Raman Spectroscopy of Pyocyanin Secreted by Pseudomonas aeruginosa Communities. *Langmuir* **2019**, *35* (21), 7043−7049.
(38) Bindesri, S. D.; Alhatab, D. S.; Brosseau, C. L. Development of an electrochemical surface-enhanced Raman spectroscopy (EC-SERS) fabric-based plasmonic sensor for point-of-care diagnostics. *Analyst* **2018**, *143* (17), 4128−4135.
(39) Yuan, T.; Ngoc, L. L. T.; van Nieuwkasteele, J.; Odijk, M.; van den Berg, A.; Permentier, H.; Bischoff, R.; Carlen, E. T. In Situ Surface-Enhanced Raman Spectroelectrochemical Analysis System with a Hemin Modified Nanostructured Gold Surface. *Anal. Chem.* **2015**, *87*, 2588−2592.
(40) Isogai, T.; Motobayashi, K.; Ikeda, K. A single spectroscopic probe for in situ analysis of electronic and vibrational information at both sides of electrode/electrolyte interfaces using surface-enhanced Raman scattering. *J. Chem. Phys.* **2021**, *155* (20), 204702.
(41) Hill, C. M.; Bennett, R.; Zhou, C.; Street, S.; Zheng, J.; Pan, S. Single Ag nanoparticle spectroelectrochemistry via dark-field scattering and fluorescence microscopies. *J. Phys. Chem. C* **2015**, *119* (12), 6760−6768.
(42) Searles, E. K.; Gomez, E.; Lee, S.; Ostovar, B.; Link, S.; Landes, C. F. Single-Particle Photoluminescence and Dark-Field Scattering during Charge Density Tuning. *J. Phys. Chem. Lett.* **2023**, *14*, 318−325.
(43) Isogai, T.; Motobayashi, K.; Ikeda, K. A single spectroscopic probe for in situ analysis of electronic and vibrational information at both sides of electrode/electrolyte interfaces using surface-enhanced Raman scattering. *J. Chem. Phys.* **2021**, *155* (20), 204702.
(44) Nam, W.; Ren, X.; Kim, I.; Strobl, J.; Agah, M.; Zhou, W. Plasmonically Calibrated Label-Free Surface-Enhanced Raman Spectroscopy for Improved Multivariate Analysis of Living Cells in Cancer Subtyping and Drug Testing. *Anal. Chem.* **2021**, *93* (10), 4601−4610.
(45) Garg, A.; Mejia, E.; Nam, W.; Vikesland, P.; Zhou, W. Biomimetic Transparent Nanoplasmonic Meshes by Reverse-Nanoimprinting for Bio-Interfaced Spatiotemporal Multimodal SERS Bioanalysis. *Small* **2022**, *18* (45), 2204517.
(46) Zhou, W.; Hua, Y.; Huntington, M. D.; Odom, T. W. Delocalized Lattice Plasmon Resonances Show Dispersive Quality Factors. *J. Phys. Chem. Lett.* **2012**, *3* (10), 1381−1385.
(47) Zhou, W.; Odom, T. W. Tunable subradiant lattice plasmons by out-of-plane dipolar interactions. *Nat. Nanotechnol* **2011**, *6* (7), 423−7.
(48) Mejia, E.; Qian, Y.; Safiabadi Tali, S. A.; Song, J.; Zhou, W. Spectral tuning of double resonant nanolaminate plasmonic nanoantennas with a fixed size. *Appl. Phys. Lett.* **2021**, *118* (24), 241108.
(49) Nam, W.; Song, J.; Ali Safiabadi Tali, S.; Lezec, H. J.; Agrawal, A.; Zhou, W. Au/SiO2-Nanolaminated Plasmonic Nanoantennas as Refractive-Index-Insensitive and Transparent Surface-Enhanced Raman Spectroscopy Substrates. *Acs Applied Nano Materials* **2021**, *4*, 3175−3184.
(50) Borovkova, O. V.; Hashim, H.; Ignatyeva, D. O.; Kozhaev, M. A.; Kalish, A. N.; Dagesyan, S. A.; Shaposhnikov, A. N.; Berzhansky, V. N.; Achanta, V. G.; Panina, L. V.; Zvezdin, A. K.; Belotelov, V. I. Magnetoplasmonic structures with broken spatial symmetry for light control at normal incidence. *Phys. Rev. B* **2020**, *102* (8), 081405.
(51) Ali Safiabadi Tali, S. A. S.; Zhou, W. Multiresonant plasmonics with spatial mode overlap: overview and outlook. *Nanophotonics* **2019**, *8*, 1199−1225.
(52) Burke, L. D.; Nugent, P. F. The Electrochemistry of Gold: I The Redox Behaviour of the Metal in Aqueous Media. *Gold Bulletin* **1997**, *30* (2), 43−53.
(53) Bard, A. J.; Faulkner, L. R.; White, H. S. *Electrochemical Methods: Fundamentals and Applications*; John Wiley & Sons: New York, 2022.
(54) Freericks, J. K.; Devereaux, T. P. Raman scattering through a metal-insulator transition. *Phys. Rev. B* **2001**, *64* (12), 125110.
(55) Carles, R.; Bayle, M.; Benzo, P.; Benassayag, G.; Bonafos, C.; Cacciato, G.; Privitera, V. Plasmon-resonant Raman spectroscopy in metallic nanoparticles: Surface-enhanced scattering by electronic excitations. *Phys. Rev. B* **2015**, *92* (17), 174302.
(56) Martina, I.; Wiesinger, R.; Jembrih-Simbürger, D.; Schreiner, M. Micro-Raman characterisation of silver corrosion products: instrumental set up and reference database. *E-Preserv Sci.* **2012**, *9*, 1−8.
(57) Chan, M. Y.; Leng, W.; Vikesland, P. J. Surface-Enhanced Raman Spectroscopy Characterization of Salt-Induced Aggregation of Gold Nanoparticles. *ChemPhysChem* **2018**, *19* (1), 24−28.
(58) Morales, D. M.; Risch, M. Seven steps to reliable cyclic voltammetry measurements for the determination of double layer capacitance. *J. Phys-Energy* **2021**, *3* (3), 034013.
(59) Aldous, L.; Silvester, D. S.; Villagrán, C.; Pitner, W. R.; Compton, R. G.; Lagunas, M. C.; Hardacre, C. Electrochemical studies of gold and chloride in ionic liquids. *New J. Chem.* **2006**, *30* (11), 1576−1583.
(60) Garrell, R. L.; Beer, K. D. Surface-enhanced Raman scattering from 4-ethylpyridine and poly (4-vinylpyridine) on gold and silver electrodes. *Langmuir* **1989**, *5* (2), 452−458.
(61) Ali Safiabadi Tali, S.; Song, J.; Nam, W.; Zhou, W. Two-Tier Nanolaminate Plasmonic Crystals for Broadband Multiresonant Light Concentration with Spatial Mode Overlap. *Advanced Optical Materials* **2021**, *9*, 2001908.
(62) Stefancu, A.; Lee, S.; Zhu, L.; Liu, M.; Lucacel, R. C.; Cortes, E.; Leopold, N. Fermi Level Equilibration at the Metal-Molecule

https://doi.org/10.1021/acsnano.3c01491
ACS Nano 2023, 17, 8634−8645

Interface in Plasmonic Systems. *Nano Lett.* **2021**, *21* (15), 6592−6599.
(63) Huang, J.; Li, P.; Chen, S. L. Potential of zero charge and surface charging relation of metal-solution interphases from a constant-potential jellium-Poisson-Boltzmann model. *Phys. Rev. B* **2020**, *101* (12), 125422.
(64) Wakatsuki, T.; Furukawa, H.; Kawaguchi, K. Specific and non-specific adsorption of inorganic ions I. Evaluation of specific adsorbability by means of minimum concentration for specific adsorption. *Soil Science and Plant Nutrition* **1974**, *20* (4), 353−362.
(65) Stefancu, A.; Lee, S.; Zhu, L.; Liu, M.; Lucacel, R. C.; Cortés, E.; Leopold, N. Fermi level equilibration at the metal−molecule interface in plasmonic systems. *Nano Lett.* **2021**, *21* (15), 6592−6599.
(66) Sigle, D. O.; Mertens, J.; Herrmann, L. O.; Bowman, R. W.; Ithurria, S.; Dubertret, B.; Shi, Y.; Yang, H. Y.; Tserkezis, C.; Aizpurua, J.; Baumberg, J. J. Monitoring morphological changes in 2D monolayer semiconductors using atom-thick plasmonic nanocavities. *ACS Nano* **2015**, *9* (1), 825−30.
(67) Tazi, S.; Salanne, M.; Simon, C.; Turq, P.; Pounds, M.; Madden, P. A. Potential-Induced Ordering Transition of the Adsorbed Layer at the Ionic Liquid/Electrified Metal Interface. *J. Phys. Chem. B* **2010**, *114* (25), 8453−8459.
(68) Merlet, C.; Limmer, D. T.; Salanne, M.; van Roij, R.; Madden, P. A.; Chandler, D.; Rotenberg, B. The Electric Double Layer Has a Life of Its Own. *J. Phys. Chem. C* **2014**, *118* (32), 18291−18298.
(69) Yan, P.; Acker, C. D.; Loew, L. M. Tethered Bichromophoric Fluorophore Quencher Voltage Sensitive Dyes. *ACS Sens* **2018**, *3* (12), 2621−2628.
(70) Balch, H. B.; McGuire, A. F.; Horng, J.; Tsai, H. Z.; Qi, K. K.; Duh, Y. S.; Forrester, P. R.; Crommie, M. F.; Cui, B.; Wang, F. Graphene Electric Field Sensor Enables Single Shot Label-Free Imaging of Bioelectric Potentials. *Nano Lett.* **2021**, *21* (12), 4944−4949.
(71) Habib, A.; Zhu, X.; Can, U. I.; McLanahan, M. L.; Zorlutuna, P.; Yanik, A. A. Electro-plasmonic nanoantenna: A nonfluorescent optical probe for ultrasensitive label-free detection of electro-physiological signals. *Sci. Adv.* **2019**, *5*, eaav9786.
(72) Novo, C.; Funston, A. M.; Gooding, A. K.; Mulvaney, P. Electrochemical charging of single gold nanorods. *J. Am. Chem. Soc.* **2009**, *131* (41), 14664−6.
(73) Johnson, P. B.; Christy, R.-W. Optical constants of the noble metals. *Phys. Rev. B* **1972**, *6* (12), 4370.

https://doi.org/10.1021/acsnano.3c01491
ACS Nano 2023, 17, 8634−8645